Dalton Transactions

Accepted Manuscript

ROYAL SOCIETY OF CHEMISTRY

www.rsc.org/dalton

Hybrid ZnO/ZnS nanoforests as the electrode materials for high performance supercapacitor application

Siwen Zhang[a], Bosi Yin[a], He Jiang[a], Fengyu Qu[a], Ahmad Umar[b,c,*], Xiang Wu[a,*]

[a]Key Laboratory for Photonic and Electronic Bandgap Materials, Ministry of Education, Harbin Normal University, Harbin 150025, P. R. China

[b]Promising Centre for Sensors and Electronic Devices (PCSED) and [c]Department of Chemistry, College of Science and Arts, Najran University, Najran 11001, Kingdom of Saudi Arabia

Any correspondences should be addressed: E-mail: wuxiang05@gmail.com; ahmadumar786@gmail.com

Heterostructured ZnO/ZnS nanoforests are prepared through a simple two-step thermal evaporation method at 650 ^{o}C and 1300 ^{o}C in a tube furnace under the flow of argon gas, respectively. A metal catalyst (Au) to form a binary alloy has been used in the process. The as-obtained ZnO/ZnS products are characterized by using a series of techniques, including scanning electron microscope (SEM), X-ray diffraction (XRD), energy dispersion X-ray spectrum (EDS), Raman spectrum and photoluminescence. A possible growth mechanism is temporarily proposed. The hybrid structures are also directly functionalized as supercapacitors (SCs) electrode without using any ancillary materials such as carbon black or binder. Results show the as-synthesized ZnO/ZnS heterostructures exhibit a greatly reduced ultraviolet emission and dramatically enhanced green emission compared to pure ZnO nanorods. The SCs data demonstrate high specific capacitance of 217 mF/cm^2 at 1 mA/cm^2 and excellent cyclic performance with 82 % capacity retention after 2000 cycles at a current density of 2.0 mA/cm^2.

1. Introduction

ZnS and ZnO are two important II-VI wide bandgap semiconductors. Nanostructured ZnS and ZnO materials have attracted considerable interest due to their sizes, morphology-related properties and wide-ranging applications, such as lasers,[1,2] sensors,[3,4] transistors,[5] nanogenerators,[6] photodetectors[7-9] and photocatalysts.[10-12] In recent years, nanoscale ZnO/ZnS heterostructures with different morphologies such as nanobelts,[13-14] nanofilms,[15] nanorings[16-17] have been reported. These morphologies can be obtained by thermal evaporation method,[18-20] hydrothermal route [21-23] and self-assembly of nanoparticles.[24,25] Among the above mentioned methods, chemical vapor deposition (CVD) method is a very facile method because of its facile handling of the process. In literature, Wang's group reported rectangular porous ZnO/ZnS nanocables and ZnS nanotubes and studied their photoluminescence properties.[26] Fang and his coworkers investigated cathodoluminescence of individual ZnS/ZnO biaxial nanobelt heterostructure.[19] Meng et al. synthesized three-dimensional hetero-epitaxial ZnO/ZnS core/shell nanorod and studied their cathodoluminescence.[24] Wang studied photocatalytic H_2 production of ZnO/ZnS core/shell nanorods.[27] Lo's group fabricated the electrode of dye-sensitized solar cells using hollow ZnS/ZnO/ZnS nanostructure, and studied effect of multiple scattering of ZnS-ZnO-ZnS interface on increasing the optical path length.[21]

However, to the best of our knowledge, there are not any reports about electrochemical properties of ZnO/ZnS nano-heterostructure as the supercapacitor electrode. In this paper, we prepared large scale heterostructured ZnO/ZnS

nanoforests by a simple two-step vapor-phase transport method. The prepared nanoforests were investigated in detail in terms of their morphological, structural and optical properties. The hybrid heterostructures are used as supercapacitor electrode and the corresponding electrochemical properties are investigated, revealing their superiority to single ZnO or ZnS nanostructures.

2. Experimental

2.1 Synthesis of ZnO Nanorod Arrays The samples were synthesized in a conventional horizontal tube furnace. First, a piece of silicon wafer was immersed into acetone solution, ultrasonically cleaned for 30 min and rinsed with deionized water. Then1.5 g Zn powder (Alfa Aesar, 99.99% purity) was put into an alumina boat and the alumina boat was covered with a piece of silicon wafer. The boat was then put at the center zone of a quartz tube. After pumping the pressure in the tube to 0.1 MPa, oxygen gas with a constant rate of 80 sccm was supplied in whole process. Then the furnace was heated to 650 ^{o}C and maintained for 90 min. After that, the furnace was naturally cooled down to room temperature.

2.2 Synthesis of Hetero-Epitaxial ZnO/ZnS Nanoforests The mixture of 0.4g ZnS powder (Alfa Aesar, 99.99% purity), 0.05g carbon powder and 0.05g In_2O_3 powder were put in the center zone of the quartz tube and the silicon wafer covered with ZnO nanorods was put at a lower temperature zone of the quartz tube for the substrate. Argon with a constant rate of 50 sccm was input into the tube. The furnace was heated to 1200 ^{o}C in 115 min and kept for 90 min. The experiment with a pure silicon wafer as the substrate was also conducted for the comparation.

The obtained product was characterized by scanning electron microscope (SEM, Hitachi-4800), X-ray powder diffraction (XRD, Rigaku Dmax-rB, Cu Kα radiation, λ = 0.1542 nm, 40 KV, 100 mA). Optical property of the as-synthesized nanoforests was investigated by photoluminescence spectroscopy (PL SPEX FL-2T2) and Raman spectroscopy (HR800).

All electrochemical measurements were carried out with a CHI 660 electrochemical workstation in a conventional three electrode cell with 1 M KOH aqueous solution as the electrolyte. ZnO/ZnS nanoforests supported on 1×1 cm^2 silicon wafer, a platinum plate and a saturated calomel electrode (SCE) electrode were used as the working electrode, counter and reference electrode, respectively.

Results and Discussion

The crystallinity and crystal phases of the as-prepared three products are first examined by X-ray diffraction and the results are demonstrated in Figure 1. From blue curve, the typical diffraction peaks of hexagonal ZnO structure (PDF no. 36-1451) indicate that the nanorods consist of pure single crystalline ZnO. When reaction time is 90 min, the diffraction peak of ZnO is still very strong with some peaks of ZnS (PDF no. 36-1450), as demonstrated in red curve. In addition, for ZnS flower-like structure, only the diffraction peak of ZnS can be found, no characteristic peaks of the other impurities are found, implying the as-synthesized product possesses high purity.

The morphologies and crystalline structure of the as-synthesized nanoforests are shown in Figure 2. From low magnification SEM image in Figure 2a, it can be seen that many nanorod arrays are successfully prepared. Figure 2b and c show high

magnification SEM images of the as-product, finding that some nanosheets were inlayed on the surface of each rod, the nanorods rank in order, like the forests, named as the nanoforests. The nanorod possesses an average diameter of 1.5 μm and a length of hundreds of micrometers. The inset image shown in Figure 2c represents the EDS spectrum of red line, indicate that only Zn and S elements exist in the nanosheets, indicating the formation of pure ZnS structures. EDS spectrum (line scanning in the zone labeled in Figure 2c) of the nanorod shows only Zn, S and O appear, as shown in Figure 2d.

Figure S1 shows SEM image of pure ZnO nanorods. Figure S1a shows low magnification SEM images of the product grown on silicon wafer. One can find that large quantities flowerlike structures consisting of many nanorods covered on the substrate. Figure S1b and S1c exhibit typical high magnification SEM images. The average diameter of the nanorod is 3 μm and the length is up to tens of micrometers. Energy dispersive X-ray (EDX) analysis in Figure S1d further proves the existence of only Zn and O elements in the ZnO nanorods. The atom ratio of Zn and O is 1:0.9, which agrees well with the theoretical value of ZnO.

When we conducted the experiment to grow ZnO/ZnS nanoforests, the silicon wafer covering ZnO nanorods is used as the substrate. The experiment with a pure silicon wafer as the substrate was also conducted for the comparation. SEM images of the as-synthesized products are shown in Figure S2a and 2b. It can be clearly seen that some microflowers consisting of many nanosheets covered on Si substrate. High magnification SEM images showed that the diameter of each microflower is about 15

μm. EDS spectrum shown in Figure S2c, indicate that only Zn and S elements exist in the microflower, indicating the formation of pure ZnS structures. On the basis of the aforementioned experimental results, the growth of ZnS microflowers may be governed by VS process, and a possible mechanism was proposed. As illustrated in Figure S2d. When the mixture of ZnS and In_2O_3 is heated to 1200 ^oC, ZnS vapor formed and deposited directly on the Si substrate to form ZnS crystalline nuclei via VS process. ZnS crystalline nuclei grew into thick nanosheets due to the local segregation of the doping element of indium, as a result, ZnS thick nanosheet films are obtained.[28] Moreover, because of the large surface energy, the new formed nuclei would spontaneously "land"on the as-formed sheets and further grow to another sheet. The assembled ZnS nanosheets continue to grow with time being prolonged to 90 min. Thus, flower-like ZnS architectures were formed.

The growth mechanism for ZnO/ZnS nanoforests might be proposed as follow. Figure 3 shows the schematic for the formation of ZnO/ZnS nanoforests. First, Zn vapor can be dissolved in Au nanoparticle catalyst to form Zn-Au alloy. When the solubility of Zn vapor in Au nuclei reaches supersaturation, Zn can overflow from the Au nuclei and react with oxygen in the closed system to form ZnO nuclei at the catalyst interface. Subsequently, ZnO nuclei assemble in a hexagonal shape and grow into the nanorod on the substrate. In the second step reaction, ZnS powder was evaporated into ZnS vapor first and flowed to the downward by carrier gases and nucleated in the deposition substrate on which ZnO arrays grown. With the reaction proceeding, In_2O_3 coated on the surface of the substrate can be evaporated

into In vapor in the temperature of 1200 ^{o}C. During the growth process of ZnO spine, due to high free energy in the side of spine, In vapor can be condensed in both sides as the site of nucleation to promote secondary growth[29] and finally inducing formation of complex nanostructures.

Figure 4 shows the corresponding Raman spectra of these three samples, which give further evidence for the crystallization, structural disorder and defects. Five peaks of the as-obtained ZnO nanorods (blue line) are observed at 332, 379, 439, 535 and 585 cm^{-1}, respectively. The peak at 439 cm^{-1} is assigned to E_2 optical phonon, which corresponds to the band characteristic of ZnO wurtzite hexagonal phase.[30] The peaks located at 535 cm^{-1} and 585 cm^{-1} correspond to LO phonon of A_1 and E_1, respectively. Besides these "classical" Raman modes, weaker peaks at 332 cm^{-1} and 379 cm^{-1} can be assigned to A_1(TO) and E_1(TO) modes of ZnO, respectively.[19] There is only one main Raman peak in the ZnO/ZnS nanoforest (black line). Raman peaks located at 350 cm^{-1}, which corresponds well to the first order LO phonon modes in ZnS. [31] Raman spectrum of pure ZnS (red line) shows six peaks centered at 217, 276, 350, 413, 443 and 670 cm^{-1}, respectively. Two peaks observed at 276 and 350 cm^{-1} can be assigned to E_1(TO) and A_1(LO) phonon modes of ZnS, respectively. The modes at 217, 413 and 443 cm^{-1} are due to the first-order and second zone-boundary phonons. A much weaker and broader band near 670 cm^{-1} can be associated with the second-order LO phonon.[32]

To further investigate the microstructure of these nanostructures, room temperature PL experiments of three products are conducted. Figure 5 presents PL

spectra of ZnO nanorods, ZnO/ZnS nanoforest and ZnS microflowers. A UV emission peak at 380 nm along with a broad green emission centered at around 522 nm was observed in ZnO nanorods. It is generally believed that the UV emission originates from the recombination of free excitons in near band edge of wide band gap ZnO.[33] and the broad visible luminescence has commonly been attributed to the recombination of a photogenerated hole with the single ionized charged state of the defect.[34, 35] PL spectrum of ZnO/ZnS nanoforest shows an enhanced UV emission peak with a small red shift as compared to pure ZnO nanorods. The red shift of UV emission can be attributed to the strain caused by lattice mismatch between ZnO and ZnS.[36] Moreover, a wide band gap semiconductor material (ZnS) coated on the surface of ZnO passivates the surface electronic states of ZnO nanorods, resulting in an obvious enhancement in UV luminescence.[37] To pure ZnS product, we find a strong peak at 415 nm and a weak peak at 552 nm. The radiative recombination on surface of ZnS nanocrystals with sulfur vacancies is responsible for the defect emission with a maximum at about 415 nm.[38] In our previous work, we thought gold catalyst results in the emission.[39] Here we use silicon substrate without any catalysts, therefore the weak emission at 552 nm could be ascribed to some self-activated centers, vacancy states or interstitial states.[40, 41]

To test the electrochemical capacitive performance of ZnO/ZnS structures, cyclic voltammogram (CV) was firstly recorded. Figure 6a presents CV curves of ZnO/ZnS sample in the potential window of 0.6 to 1.3 V at different scan rates of 10, 20, 30, 50, and 100 mVs^{-1}. Specifically, a series of redox peaks are observed within

the potential range from 0.6 to 1.3 V for all scan rates, which correspond to the conversion between different valence states as follows:[42, 43]

$$ZnS + OH^- \leftrightarrow ZnSOH + e^- \quad (1)$$

$$ZnSOH + OH^- \leftrightarrow ZnSO + H_2O + 2e^- \quad (2)$$

The peak currents increase a lot as the scan rates increase, suggesting that the ZnO/ZnS architectures possess fast charge transfer and anion diffusion ability. Figure 6b shows the charge-discharge curves of the as-prepared samples at different current densities. Clearly, with current density increasing, the charge-discharge time reduces. The areal capacitances (C_a) calculated from these charge-discharge curves are according to the following equation[44]

$$C_a = I\Delta t/S\Delta E$$

where I is the charge-discharge current, Δ t is the charge-discharge time, Δ E is the potential window during the charge-discharge process (exclude IR drop), and S is the effective electrode area. The areal capacitance of ZnO/ZnS electrode is as high as 217 mF/cm^2 at the current density of $1mA/cm^2$, as shown in Figure 6c. Figure 6d demonstrates cycling performance of the electrode material up to 2000 cycles at the current density of 2.0 mA/cm^2. No obvious specific capacitance loss was observed, revealing its excellent long-term cycling stability.

The capacitive performance of the as-prepared pure ZnO nanorods was also evaluated, as shown in Figure S3. Redox peaks at various scan rates don't appear in the CV curves of pure ZnO (Figure S3a). So, we think that redox peaks from ZnO/ZnS nanoforest might come from ZnS. Figure S3b shows the charge-discharge

curves of the as-prepared ZnO samples at different current densities. It is observed that the charge-discharge time is shorter than that of ZnO/ZnS nanoforest. The area capacitance plots derived from the galvanostatic charge-discharge measurements in different current densities are shown in Figure S3c. The area capacitances were measured to be 43, 32, 5.3, 3.4, and 2.4 mF/cm^2 at 1, 1.2, 1.5, 2 and 5 mA/cm^2, respectively. Only 6% of capacitance was retained when the current density increased from 1 to 5 mA/cm^2. Figure S3d demonstrates cycling performance of the electrode material up to 2000 cycles at the current density of 2.0 mA/cm^2.

Finally, the capacitive performance of ZnS microflowers is also measured. Figure S4a shows the CV curves of ZnS microflowers. Redox peaks could be readily observed. This proved again that redox reaction happened in ZnS structures. Figure S4b shows the charge-discharge curves of the as-prepared samples at different current densities. The area capacitance plots derived from the galvanostatic charge-discharge measurements in different current densities are shown in Figure S4c. Figure S4d demonstrates the cycling performance of the electrode material up to 2000 cycles at the current density of 2.0 mA/cm^2. In other words, The capacitive performance of pure ZnS is not superior to ZnO/ZnS nanoforests.

Figure 7a shows the cyclic voltammetry (CV) curves of ZnO/ZnS nanoforests, ZnO nanorods and ZnS microflowers electrodes collected at the scan rate of 100 mV/s. CV area of ZnO/ZnS electrode is much larger than ZnO and ZnS electrodes, suggesting ZnO/ZnS electrode possesses a larger specific capacitance. Typical galvanostatic charge-discharge curves of different electrodes collected at a current

density of 1.0 mA/cm^2 are shown in Figure 7b. The charge-discharge curve of ZnO/ZnS electrode prolongs over ZnO and ZnS electrodes. The areal capacitance of ZnO/ZnS sample is significantly higher than those of ZnO and ZnS electrodes. Figure 7c is the summary of the areal capacitance vs current density for the three different materials. It is clearly shown that the areal capacitances of the pseudocapacitors increase in the order of ZnS < ZnO < ZnO/ZnS. For example, at the same current density of 1.0 mA/cm^2, the areal capacitance for ZnO/ZnS pseudocapacitors (217mF/cm^2) is higher than that of ZnO pseudocapacitors (43 mF/cm^2) and ZnS pseudocapacitors (36.5 mF/cm^2). The cycling performance of three different materials as the pseudocapacitor electrodes demonstrates the degradation of the capacitance with the cycle number (Figure 7d). When cycling experiments are conducted at the same current density of 2.0 mA/cm^2, the retained capacitance of ZnO/ZnS pseudocapacitor is much higher than the other twos, demonstrating that the ZnO/ZnS nanoforests electrode is more suitable than the others.

4. Conclusions

In summary, hybrid ZnO/ZnS nanoforests were prepared via a simple two-step thermal evaporation method. The electrochemical performances of the as-obtained products as supercapacitor electrodes were systematically investigated. The results show that ZnO/ZnS nanoforests exhibit much higher areal capacitance than the other two materials. CVs and galvanostatic charge-discharge measurements indicate that ZnO/ZnS nanoforests shows high capacitance of about 217 mF/cm^2 in a 1 M KOH electrolyte and stays at 177 mF/cm^2 after 2000 cycles at a current density of 2.0

mA/cm^2. The as-prepared ZnO/ZnS nanoforests are promising as the electrodes for high-performance supercapacitor applications.

Acknowledgement

This work was supported by the Scientific Research Fund of Heilongjiang Provincial Education Department (12531179) and Program for Scientific and Technological Innovation Team Construction in Universities of Heilongjiang (No. 2011TD010).

References

1. M. H. Huang, S. Mao, H. Feick, H. Q. Yan, Y. Y. Wu, H. Kind, E. Weber, R. Russo and P. D. Yang, Science, 2001, **292**, 1897.
2. X. F. Duan, Y. Huang, R. Agarwal and C. M. Lieber, Nature, 2003,**421**,241.
3. X. S. Fang, Y. S Bando, M. Y. Liao, U. Gautam, C. Y. Zhi, B. Dierre, B. D. Liu, T. Y. Zhai, T. Sekiguchi, Y. Koide and D. Golberg, Adv. Mater. 2009, **21**, 2034.
4. Y. Cui, Q. Q. Wei, H. K. Park and C. M. Lieber, Science, 2001, **293**, 1289.
5. H. B. Chen, X. Wu, L. H. Gong, C. Ye, F. Y. Qu and G. Z. Shen, Nanoscale Res. Lett, 2010, **5**, 570.
6. Z. L.Wang and J. H. Song, Science, 2006, **312**, 242.
7. X. S. Fang, L. F. Hu, K. F. Huo, B. Gao, L. J. Zhao, M. Y. Liao, P. K. Chu, Y. Bando and D. Golberg, Adv. Funct. Mater, 2011, **21**, 3907.
8. X. S. Fang, S. L. Xiong, T. Y. Zhai, Y. Bando, M. Y. Liao, U. K. Gautam,Y. Koide, X. G. Zhang, Y. T. Qian and D. Golberg, Adv. Mater, 2009, **21**, 5016.
9. M. Chen, L. F. Hu, J. X. Xu, M. Y. Liao, L. M. Wu and X. S. Fang, Small 2011, **7**, 2449.

10. J. Wang, F. Y. Qu and X. Wu, Sci. Adv. Mater, 2013, **5**, 1364.

11. J. Wang, F. Y. Qu and X. Wu, Sci. Adv. Mater, 2013, **5**, 1052.

12. W. N. Jia, X. Wu, B. X. Jia, F. Y. Qu and H. J. Fan, Sci. Adv. Mater, 2013, **5**, 1329.

13. L. F. Hu, J. Yan, M. Y. Liao, H. J. Xiang, X. G. Gong, L. D. Zhang and X. S. Fang, Adv. Mater, 2012, **24**, 2305.

14. X. S. Fang, Y. Bando, M. Y. Liao, T. Y. Zhai, U. Gautam, L. Li, Y. Koide and D. Golberg, Adv. Funct. Mater. 2010, **20**, 500.

15. A. K. Giri, C. Charan, A. Saha, V. K. Shahi and A. B. Panda, J. Mater. Chem. A, 2014, **2**, 16997.

16. Z. Q. Liu, X. H. Lu, S. L. Xie, J. H. Zhang, Z. L. Liu and Y. X. Tong, J. Electrochem. Soc. 2011, **158**, E84.

17. X. Wu, P. Jiang, Y. Ding, W. Cai, S. S. Xie and Z. L.Wang, Adv. Mater, 2007, **19**, 2319.

18. X. Fan, M. L. Zhang, fiq, I..Sha, W. J. Zhang, C. S. Lee and S. T. Lee, Adv. Mater, 2009, **21**, 2393.

19. J. Yan, X. S. Fang, L. D. Zhang, Y. Bando, U. K. Gautam, B. Dierre, T. Sekiguchi and D. Golberg, Nano Lett, 2008, **8**, 2794.

20. X. S. Fang, T. Y. Zhai, U. K. Gautam, L. Li, L. M. Wu, Y. Bando, D. Golberg, Prog. Mater. Sci. 2011, **56**, 175.

21. S. S. Lo, Y. T. Hung and D. J. Jan, J. Mater. Chem, A. 2013, **1**, 10274.

22. W. N. Jia, B. X. Jia, F. Y. Qu and X. Wu, Dalton. Trans, 2013, **42**, 14178.

23. P. H. Guo, J. G. Jiang, S. H. Shen and L. J. Guo, Inter. J. Hydrogen Energy, 2013,

38, 13097.

24. X. Huang, M. Wang, M. Willinger, L. D. Shao, D. S. Su and X. M. Meng, ACS Nano, 2012, **8**, 7333.
25. Y. H. Ni, S. Yang, J. M. Hong, L. Zhang, W. L. Wu and Z. S.Yang, J. Phys. Chem. C, 2008, **112**, 8200.
26. X. D. Wang, P. X. Gao, J. Li, C. J. Summers, Z. L. Wang, Adv. Mater, 2002, **14**, 23
27. H. X. Sang, X. T. Wang, C. C. Fan and F. Wang, Inter. J. Hydrogen Energy, 2012, **37**, 1348.
28. F. Yang, W. H. Liu, X. W. Wang, J. Zheng, R. Y. Shi, H. Zhao and H. Q. Yang, ACS Appl. Mater. Interfaces, 2012, **4**, 3852.
29. J. Y. Lao, J. Y. Huang, D. Z. Wang and Z. F. Ren, Nano Lett, 2003, **6**, 2536.
30. T. C. Damen, S. P. S. Porto and B. Tell, Phys. Rev, 1966, **142**, 570.
31. W. G. Nilsen, Phys. Rev, 1969, **182**, 838.
32. T. Y. Zhai, Z. J. Gu, H. B. Fu, Y. Ma and J. N. Yao, Cryst. Growth. Des, 2007, **7**, 488.
33. Y. Lei, F. Y. Qu and X. Wu, Nano-Micro Lett, 2012, **4**, 45.
34. P. Chen, L. Gu and X. B. Cao, CrystEngComm, 2010,**12**, 3950.
35. X. S. Fang, C.H. Ye, L. D. Zhang, Y. H. Wang and Y. C. Wu, Adv. Funct. Mater. 2005, **15**, 63.
36. H. Liu, L. F. Hu, K. Watanabe, X. H. Hu, B. Dierre, B. Kim, T. Sekiguchi and X. S. Fang, Adv. Funct. Mater. 2013, **23**, 3701

37. X. M. Shuai and W. Z. Shen, J. Phys. Chem. C, 2011, **115**, 6415.

38. S. Sapra, A. Prakash, A. Ghangrekar, N. Periasamy and D. D. Sarma, J. Phys. Chem. B, 2005,**109**, 1663.

39. X. Wu, Y. Lei, Y. F. Zheng and F. Y. Qu, Nano-Micro Lett, 2010, **2**, 272.

40. C. H. Ye, X. S. Fang, G. H. Li and L. D. Zhang, Appl. Phys. Lett, 2004, **85**, 3035.

41. G. Z. Shen, Y. Bando and D. Golberg, Appl. Phys. Lett. 2006, **88,** 123107.

42. J. Pu, F. L. Cui, S. B. Chu, T. T. Wang, E. H. Sheng and Z. H. Wang, ACS Sustainable Chem. Engn., 2014, **2**, 809.

43. J. Xu, Q. F. Wang, X. W. Wang, Q. Y. Xiang, B. Liang, Di. Chen and G. Z. Shen, ACS nano, 2013, **7**, 5453.

44. P. H. Yang, X. Xiao, Y. Z. Li, Y. Ding, P. F. Qiang, X. H. Tan, W. J. Mai, Z. J. Lin, W. Z. Wu, T. Q. Li, H. Y. Jin, P. Y. Liu, J. Zhou, C. P. Wong and Z. L. Wang, ACS nano, 2013, **7**, 2617.

Figure captions

Figure 1: Typical XRD patterns of as-grown (a) ZnO urchins; (b) ZnS microflowers made of thin nanosheets; (c) epitaxially grown hybrid ZnO-ZnS nanoforests

Figure 2: Typical SEM images of the as-prepared epitaxially grown hybrid ZnO-ZnS nanoforests (a-b) low-resolution; (c) high-magnification SEM images; Inset (c) corresponding EDS spectrum and (d) EDX line scan for Zn, S, and O following the arrow shown in (c).

Figure 3: Plausible growth mechanism for the formation of epitaxially grown hybrid ZnO-ZnS nanoforests

Figure 4: Typical Raman-scattering spectra of as-grown (a) ZnO urchins; (b) ZnS microflowers; (c) epitaxially grown hybrid ZnO-ZnS nanoforests

Figure 5: Typical room-temperature photoluminescence (PL) spectra of as-grown (a) ZnO urchins; (b) ZnS microflowers; (c) epitaxially grown hybrid ZnO-ZnS nanoforests

Figure 6: Electrochemical characterizations of hybrid ZnO-ZnS nanoforests for supercapacitor applications using three electrodes system. (a) CV curves at scan rates between 10 and 100 mVs^{-1}; (b) charge-discharge curves at current densities ranged from 1.0 to 5.0 mA/cm^2; (c) Current density dependence of the areal capacitance; (d) Cycling performance at current density of 2.0 mA/cm^2.

Figure 7: (a) CV curves for epitaxially grown hybrid ZnO-ZnS nanoforests, ZnO urchins made of axially grown nanorods, and ZnS nanoroses made of thin ZnS nanosheets electrodes at a scan rate of 100 mV/s. (b) Galvanostatic charge-discharge

curves of hybrid ZnO-ZnS nanoforests, ZnO urchins, and ZnS nanoroses collected at a current density of 1 mA/cm^2. (c) Areal capacitances of the hybrid ZnO-ZnS nanoforests, ZnO urchins, and ZnS nanoroses based electrodes measured as a function of current density. (d) Cycling performance of hybrid ZnO-ZnS nanoforests, ZnO urchins, and ZnS nanoroses at current density of 2.0 mA/cm^2

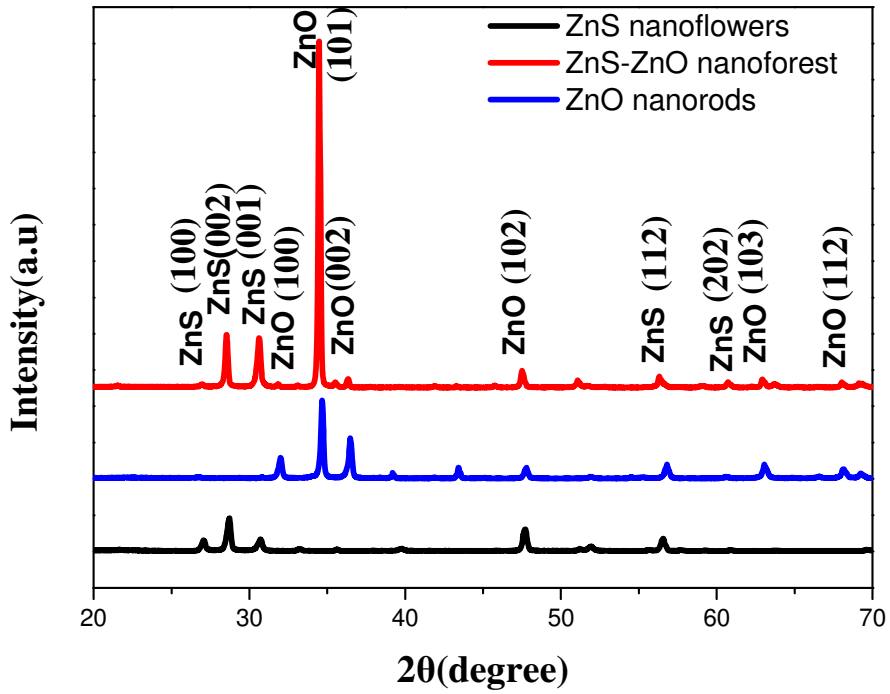

Fig. 1 Siwen Zhang et al.

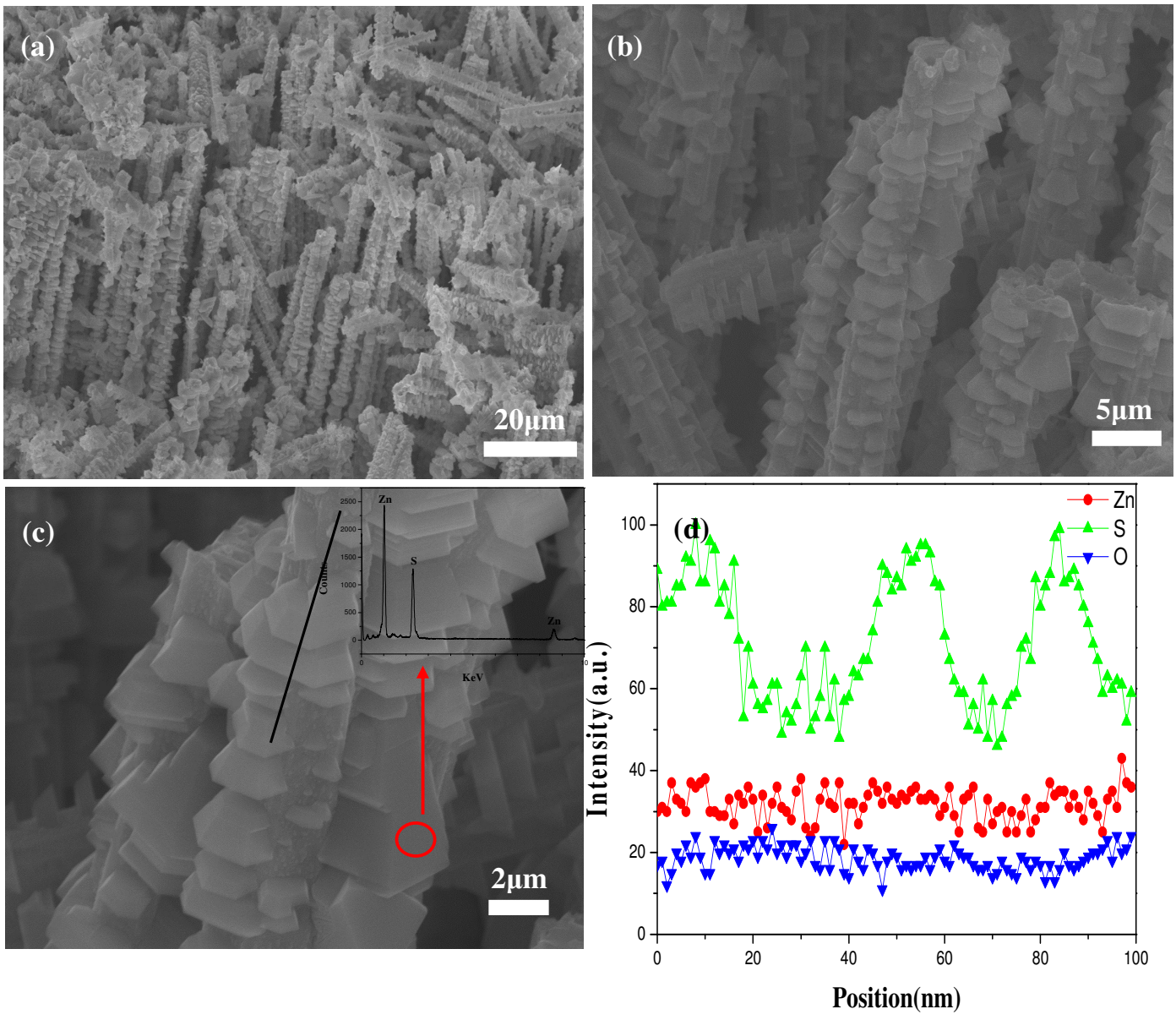

Fig. 2 Siwen Zhang et al.

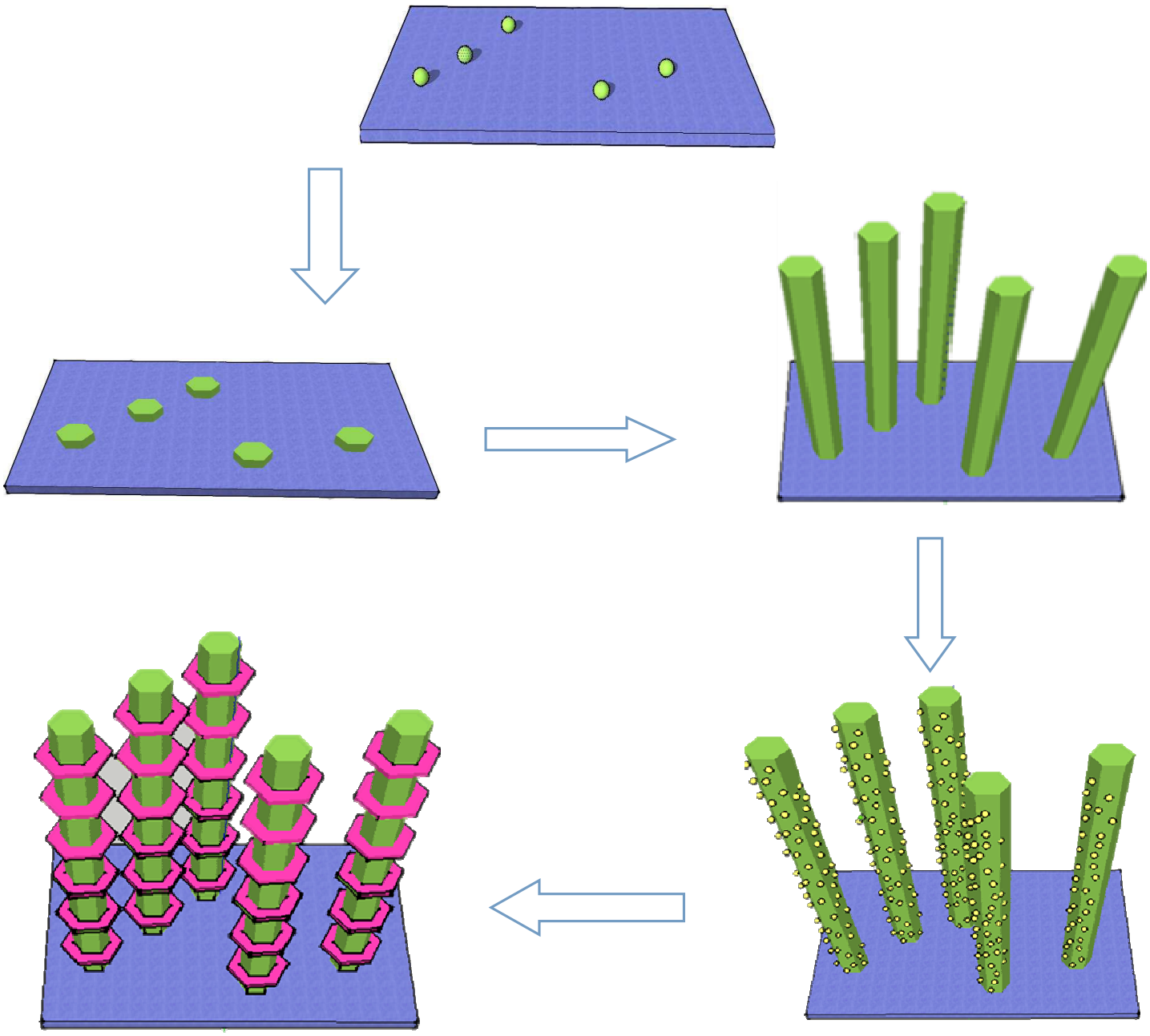

Fig. 3 Siwen Zhang et al.

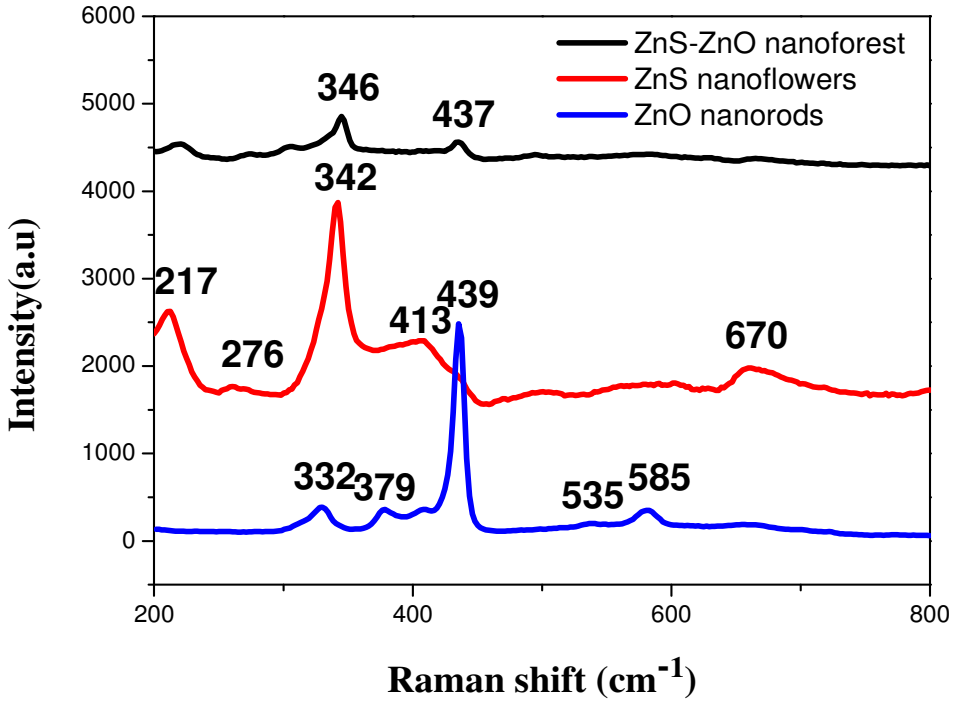

Fig. 4 Siwen Zhang et al.

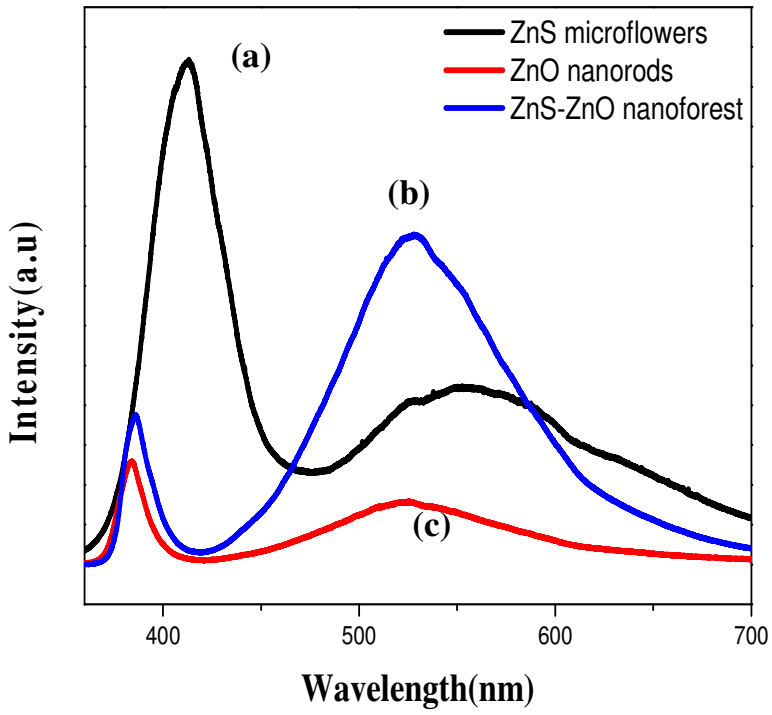

Fig. 5 Siwen Zhang et al.

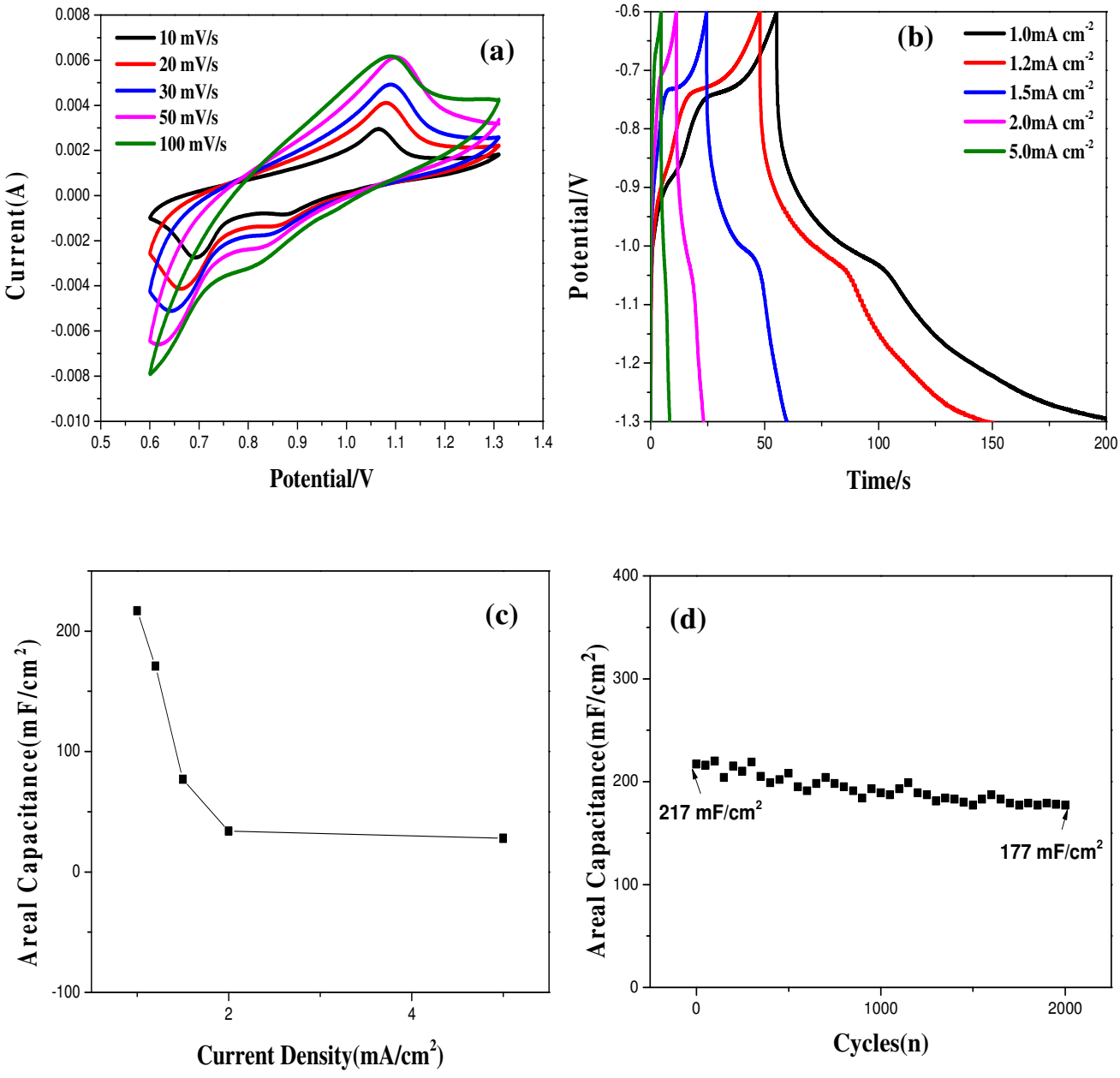

Fig. 6 Siwen Zhang et al

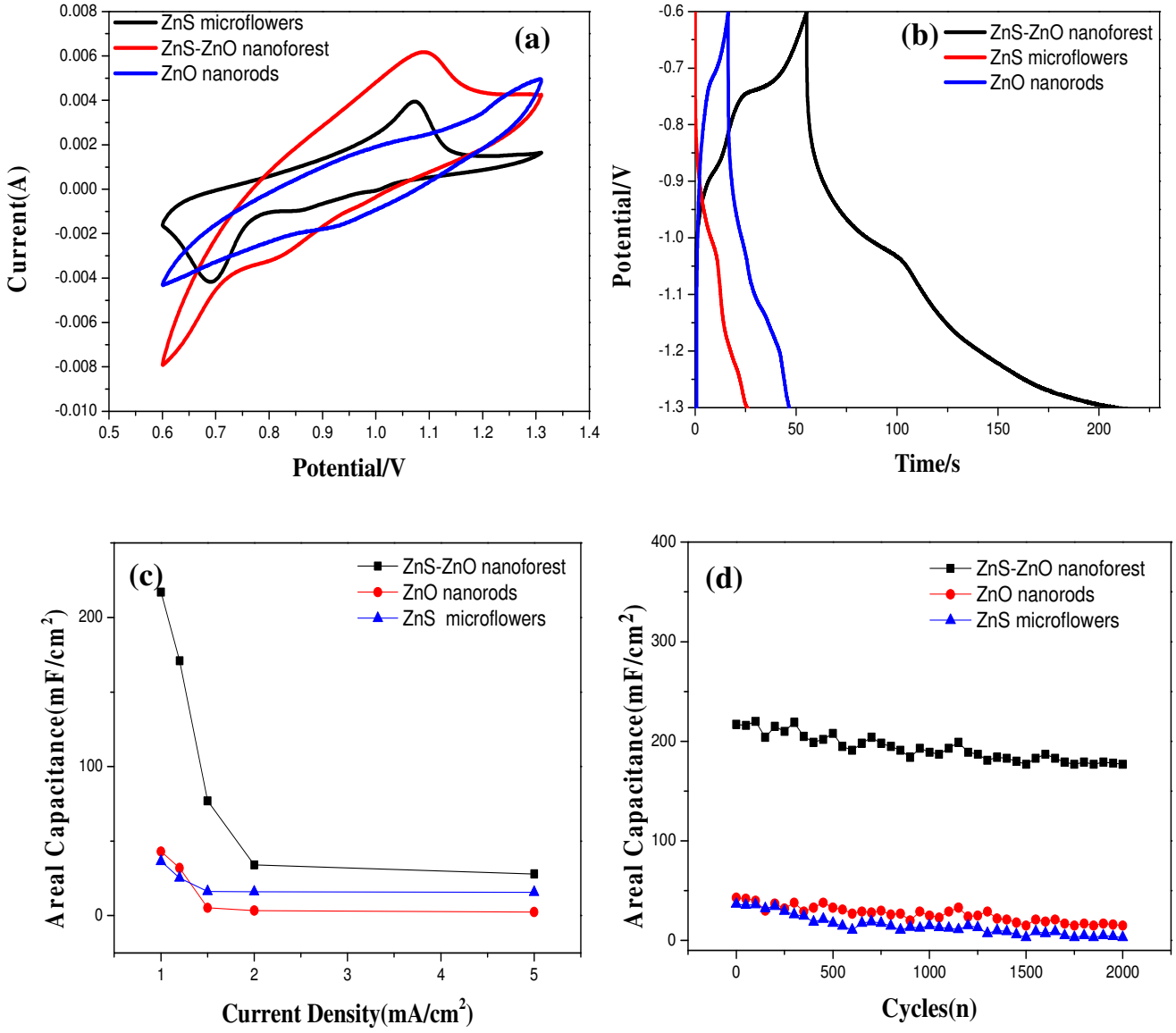

Fig. 7 Siwen Zhang et al.

Graphical Abstract